AGU100 ADVANCING EARTH AND SPACE SCIENCE

JGR

Journal of Geophysical Research: Oceans

RESEARCH ARTICLE
10.1002/2017JC013351

Key Points:
- Physical mechanism on the absorption of infrared radiation resulting in the retention of heat in a water body
- How the ocean thermal skin layer adjusts to increasing longwave radiation and winds

Correspondence to:
P. J. Minnett,
pminnett@miami.edu

Citation:
Wong, E. W., & Minnett, P. J. (2018). The response of the ocean thermal skin layer to variations in incident infrared radiation. *Journal of Geophysical Research: Oceans*, *123*, 2475–2493. https://doi.org/10.1002/2017JC013351

Received 13 AUG 2017
Accepted 16 MAR 2018
Accepted article online 23 MAR 2018
Published online 6 APR 2018

The Response of the Ocean Thermal Skin Layer to Variations in Incident Infrared Radiation

Elizabeth W. Wong[1,2] **and Peter J. Minnett**[3]

[1]Meteorology and Physical Oceanography Program, Rosenstiel School of Marine and Atmospheric Science, Miami, FL, USA, [2]Now at Centre of Remote Imaging, Sensing and Processing, National University of Singapore, Singapore, [3]Department of Ocean Sciences, Rosenstiel School of Marine and Atmospheric Science, Miami, FL, USA

Abstract Ocean warming trends are observed and coincide with the increase in concentrations of greenhouse gases in the atmosphere resulting from human activities. At the ocean surface, most of the incoming infrared (IR) radiation is absorbed within the top micrometers of the ocean's surface where the thermal skin layer (TSL) exists. Thus, the incident IR radiation does not directly heat the upper few meters of the ocean. This paper investigates the physical mechanism between the absorption of IR radiation and its effect on heat transfer at the air-sea boundary. The hypothesis is that given the heat lost through the air-sea interface is controlled by the TSL, the TSL adjusts in response to variations in incident IR radiation to maintain the surface heat loss. This modulates the flow of heat from below and hence controls upper ocean heat content. This hypothesis is tested using the increase in incoming longwave radiation from clouds and analyzing vertical temperature profiles in the TSL retrieved from sea-surface emission spectra. The additional energy from the absorption of increasing IR radiation adjusts the curvature of the TSL such that the upward conduction of heat from the bulk of the ocean into the TSL is reduced. The additional energy absorbed within the TSL supports more of the surface heat loss. Thus, more heat beneath the TSL is retained leading to the observed increase in upper ocean heat content.

1. Introduction

The ocean's role in the climate system is very important. Oceans cover about 70% of the Earth's surface and contain 97% of all the water on Earth. The large specific heat of water and its storage capacity of carbon dioxide (compared to the atmosphere) means that the ocean acts as a heat and carbon sink, modulating the surrounding air temperatures and atmospheric carbon dioxide (Bigg et al., 2003). The time scales for changes in the vast amount of energy stored in the ocean can be of order of seconds to centuries depending on depth, interaction with the atmosphere and ocean circulation. The ocean's energy influx to the atmosphere fuels weather patterns and the climate system. Thus, the ocean's forcing of the atmosphere plays a pivotal role in the Earth's energy budget, and understanding ocean-atmosphere coupling is vital in studies of the ocean, atmosphere, and the climate system.

Given that the ocean is a large heat sink, the observed increase in upper ocean heat content (OHC) is thus a concern as this would lead to an upset of the energy budget of the Earth's climate system. Ocean warming has been shown to account for over 90% of the increase in energy accumulated in the climate system between years 1971 and 2010 (IPCC, 2014). Levitus et al. (2012) showed evidence of a consistent increase in upper OHC from 1955 to 2010 and stated that two thirds of the increase in OHC occurs in the upper 700 m from the ocean surface corresponding to an increase in the surface heat flux into the ocean of 0.27 W m^{-2} over the World Ocean, and a volume mean warming of 0.18°C while the remaining one third is accounted for in the 700–2,000 m depth range. The total calculated volume mean warming is 0.09°C indicating an average change in the surface fluxes of 0.39 W m^{-2} for the 1955–2010 period over the World Ocean. Such small changes in the average atmospheric infrared (IR) emission incident at the sea surface occurring over decades are not feasible to measure with currently available instruments.

It is understood from the greenhouse effect that the increase in atmospheric greenhouse gases (GHGs) would result in an increase in the absorption and emission of thermal IR radiation which subsequently warms the Earth's surface. The 2014 Intergovernmental Panel on Climate Change (IPCC) report states that

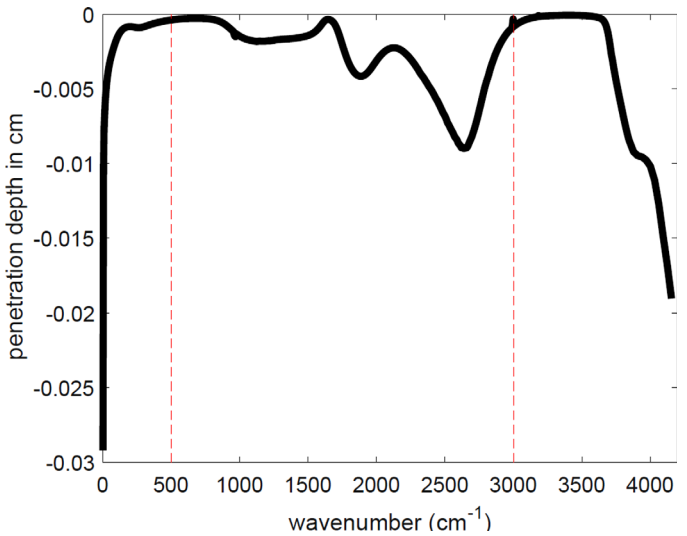

Figure 1. The penetration depth versus wave number, ν. Red dashed lines indicate $\nu = 500$ and 3,000 cm^{-1}. The penetration depth obtained from $I(-z) = I_0 \exp(-\alpha(-z))$ (equation (1)) with R_{img} obtained from Bertie and Lan (1996).

since the preindustrial era, there has been an increase in atmospheric concentrations of anthropogenic GHGs, principally carbon dioxide (CO_2), methane (CH_4), and nitrous oxide (N_2O) at a rate of 1.3%/yr from 1970 to 2000 and at 2.2%/yr from 2000 to 2010 (IPCC, 2014). The effect of this increase of GHGs on the climate system has a 95–100% probability of causing the currently observed and unprecedented warming of the climate since the mid-twentieth century. Emissions of CO_2 from the burning of fossil fuels and industrial processes are most disconcerting, contributing to about 78% of the total anthropogenic GHG increase from 1970 to 2010.

It is, however, not clear how the greenhouse effect directly affects the ocean's heat uptake in the upper 700 m of the ocean. This is because the penetration depth of IR radiation in water is within submillimeter scales (Figure 1) thereby implying that the incident longwave radiation does not directly heat the layers beyond the top submillimeter of the ocean surface. The objective of this study is therefore to understand and provide an explanation of how increasing levels of anthropogenic GHGs in the atmosphere, which raises the amounts of incident longwave radiation on the ocean surface, causes the upper OHC to rise. Furthermore, at submillimeter scales below the air-sea interface, the mechanism for the transport of heat is through molecular conduction and not by turbulence (e.g., Soloviev & Lukas, 2014). Given the mean vertical temperature gradient of the TSL, heat typically flows from the ocean to the atmosphere, therefore heat from the absorption of longwave radiation will be conducted upward, back to the sea surface. This raises questions about the cause of the observed increase in upper OHC as it suggests that all heat due to the absorption of increased longwave radiation should be concentrated in the upper submillimeter from the interface. We hypothesize that variations in the temperature gradient within the TSL, which is directly affected by the absorption and emission of longwave radiation, modulates the amount of heat loss from the air-sea interface. Thus, any changes in the vertical temperature gradient in the TSL due to variations in the absorbed longwave radiation could provide an explanation of the mechanism as to how the OHC increases through the retention of heat from the absorption of solar radiation within the bulk of the ocean.

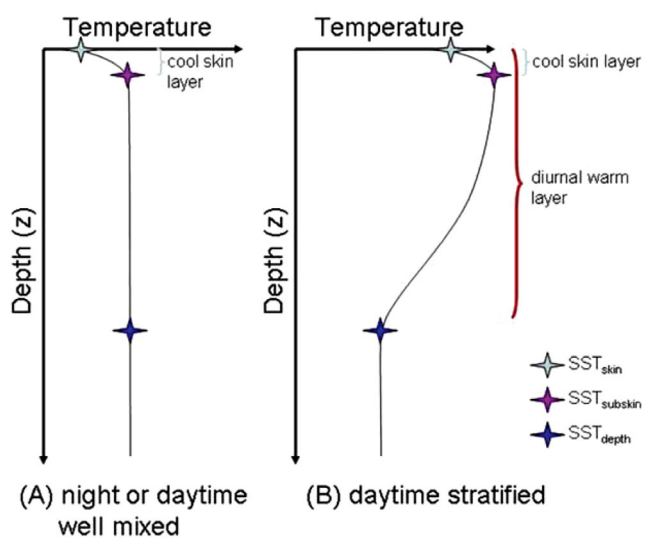

Figure 2. Cartoon of thermal skin layer during different conditions. (a) Nighttime or daytime with high wind conditions. (b) Daytime with thermal stratification resulting from the absorption of insolation in low wind speed conditions (Gentemann & Minnett, 2008).

2. Ocean Skin Layers

The near-surface ocean comprises three types of skin layers each defined by different physical processes. The first we consider is the thermal skin layer (TSL). The TSL exists directly on the aqueous side of the air-sea interface, extending to only about a tenth of a millimeter from the top of the ocean's surface (Katsaros et al., 1977; Wong & Minnett, 2016a). The direction of flow of heat is almost always from the ocean to the atmosphere meaning that the surface temperature is cooler than the temperature below the TSL (Figure 2). The temperature difference ranges from ~0.1 K during high wind speeds of >7 m s^{-1} to ~0.6 K during low wind conditions of <2.5 m s^{-1} (Donlon et al., 2002; Minnett et al., 2011). The TSL is almost always present, with occurrences of momentary disruption caused by wave breaking. Its creation and destruction are also influenced by rainfall, however, the TSL's disruption by such processes is able to completely restore itself in a matter of seconds (Jessup et al., 1997).

It is thus important that the TSL be considered during the analysis of any processes involving sea-surface temperatures (SST) and interfacial heat fluxes. This is because the energy flow down the TSL's temperature gradient sustains the latent, sensible and net IR radiative energy

Table 1
Table of the Main Properties and Depth Scales of the Three Skin Layers

	Depth scales	Properties
Thermal skin layer	~0.1 mm	Sustains the overall heat loss from ocean to atmosphere through molecular conduction.
Electromagnetic skin layer	<0.1 mm within wavelengths of 500–3,000 cm^{-1}	Due to absorption and emission of IR radiation.
Viscous skin layer	~1 mm	Viscosity suppresses turbulent velocity fluctuations.

losses by means of molecular effects (Jessup et al., 1997; McAlister & McLeish, 1969; Minnett et al., 2011). Therefore, a strong temperature gradient is established due to the poor efficiency of heat transfer by molecular conduction. The mean TSL's properties are not influenced by processes such as turbulence or convection as turbulence occurs within the ocean's mixed layer which lies beneath the TSL and convection is driven by heat flowing from the ocean surface which occurs within the atmospheric and oceanic boundary layers (Wong & Minnett, 2016a).

The second skin layer to consider is the electromagnetic (EM) skin layer. The EM skin layer exists due to EM properties of water which control the absorption and emission of IR radiation and therefore control heat losses and gains by IR radiation at the air-sea boundary. Ignoring the complicating factors of the disruption of the TSL by rain drops or the absorption of solar radiation in the TSL, the exponential profile of emission and absorption of IR radiation leads to a nonlinear TSL temperature profile (e.g., Khundzhua & Andreyev, 1974 cited in Liu & Businger, 1975) as opposed to a linear temperature profile which has been assumed by many prior studies of the TSL (e.g., Fairall et al., 1996; Saunders, 1967). The exponential decay is defined by Beer-Lambert's law, equation (1).

$$I(-z) = I_0 e^{-\alpha(-z)} \tag{1}$$

where I(–z) is the radiant intensity at depth z, I_0 is the radiant intensity at z = 0, and α is the absorption coefficient determined from the imaginary component of the refractive index of water, R_{img} ($\alpha = 4\pi\nu R_{img}$, where ν = wave number in cm^{-1}). The vertical ordinate, z, is defined positive upward with z = 0 being the ocean surface, thus all values of z are negative since we are analysing depths beneath the ocean surface and the intensity of radiation decreases with negative depth. The penetration depth, D_p, is defined as $\frac{1}{\alpha}\cos\theta$, which is indicative of the depth at which the incident radiant intensity falls to 1/e of its original value. θ is the zenith angle of propagation of an EM wave off-vertical, taking into account refraction by water at the interface. The penetration depth is also the emission depth by the time reversal symmetry of electromagnetic waves interacting with matter. Thus, from Figure 1, it is noted that the majority of the emissions originate from depths of less than 0.1 mm, within the TSL. This property is the basis of the use of IR radiometers on ships, aircraft and satellites as the radiation measured by these instruments originates from this layer thereby facilitating the estimation of surface temperatures, referred to as the skin temperature.

The viscous skin layer is the region adjacent to the air-sea interface in which turbulent velocity fluctuations are suppressed by viscosity. The flow within this layer is therefore intermittently laminar given the presence of sea-surface renewal events (Soloviev & Schlüssel, 1994). However, in this paper, we will be considering a mean viscous sublayer, therefore surface renewal events are averaged out and we only need to account for the mean viscous shear stresses. The viscous sublayer is typically of order of a millimeter (Veron et al., 2011). The TSL and EM skin layers are therefore embedded in the viscous sublayer. Table 1 highlights the main properties and depth scales of the three skin layers discussed.

Studies of the skin layers at the air-sea interface are largely directed toward obtaining the temperature difference across the TSL or depth of the viscous sublayer by using well known models which govern molecular heat fluxes and assuming a fully viscous flow close to the boundary layer (e.g., Fairall et al., 1996; Liu et al., 1979; Saunders, 1967; Soloviev & Schlüssel, 1994). However, these models do not consider the exponential decay of IR radiation. In reality, the exponential decay from the absorption and emission of radiation must be considered as this accounts for the TSL's nonlinear vertical temperature gradient (Wong & Minnett, 2016a) which is important for this study.

3. Methods

3.1. Thermal Skin Layer Temperature Profile

Wong and Minnett (2016a, 2016b) demonstrated the retrieval of the mean TSL vertical profile from spectral measurements of a highly accurate IR spectrometer, the Marine-Atmospheric Emitted Radiance Interferometer (M-AERI). The M-AERI is a sea-going, well-calibrated, Fourier Transform Infrared (FTIR) Interferometer

(Minnett et al., 2001) and was developed from the Atmospheric Emitted Radiance Interferometer (AERI; Knuteson et al., 2004) at the Space Science and Engineering Center, University of Wisconsin-Madison for the Department of Energy's Atmospheric Radiation Measurement Program (Stokes & Schwartz, 1994). The M-AERI measures radiances (units: mW m^{-2} sr^{-1} $(cm^{-1})^{-1}$) emitted in the wave number range 500–3,000 cm^{-1} (~3–20 μm in wavelength) using two IR detectors to attain this wide spectral range. It has an effective spectral resolution of 0.5 cm^{-1} that resolves many gaseous absorption and emission lines in the atmosphere (Minnett et al., 2001). The measurements of the spectra of the emission from the ocean and the atmosphere are bracketed by measurements of two internal blackbody cavities that are at well-monitored temperatures to provide real-time calibration (Minnett et al., 2001). The field of view of the M-AERI at the sea surface is ~1.1–1.5 m^2 based on an instrument installation height of 10 and 14 m above the water, and each spectrum is derived from measurements averaged over 46 s.

The radiation measured by the M-AERI when its field of view is directed toward the sea surface consists of the radiation emitted from the sea surface, $R_{sea}(\nu)$ where ν is wave number, and the reflected sky radiance, $(1-\epsilon(\nu))R_{sky}(\nu)$, where ϵ is the wave number dependent sea-surface emissivity. As the distance between the M-AERIs and sea surface is small, the contribution from atmospheric emission to our signal along this path-length is negligible. Interests lie in $R_{sea}(\nu)$ as it is emitted from the EM skin layer and thus contains information from the TSL profiles. Thus, to remove the reflected sky radiance, the spectral emissivity values, $\epsilon(\nu)$, are determined using a piecewise linear variance minimizing (VarMinT) technique (Hanafin, 2002), equation (2). The assumptions for the VarMinT are that the sky radiance, R_{sky}, is not correlated with $\epsilon(\nu)$, and $\epsilon(\nu)$ is a smooth function of ν.

$$\epsilon(\nu)=\frac{R_{sea}(\nu)-R_{sky}(\nu)}{B(\nu,T_{skin})-R_{sky}(\nu)} \tag{2}$$

After obtaining the emissivity corrected sea-surface emission spectrum, $R_{sea}(\nu)$, we can retrieve the TSL profile by solving equation 3) which consists of an integration of the radiance emitted from each infinitesimal layer attenuated by the intervening layers to the sea surface, with an attenuation factor defined by Beer-Lambert's law:

$$R_{sea}(\nu)=-\int_0^{\infty} B(\nu,T(-z))\frac{de^{\alpha(-z)}}{dz}dz \tag{3}$$

$B(\nu,T(z))$ is Planck's function with T(–z) being the vertical temperature profile of interest. The term $\frac{de^{\alpha(-z)}}{dz}$ is the weighting function given by Beer-Lambert's law. For measurements of emission with nonzero zenith angle, the path length is scaled by the cosine of the subsurface angle of propagation.

The highly nonlinear T(–z) (e.g., Liu et al.,1979) poses a problem in solving equation (3) as the equation becomes highly ill conditioned (Eyre, 1987; Rodgers, 2004). To overcome this issue, Wong and Minnett (2016a, 2016b) used the Truncated Singular Value Decomposition (TSVD) regularization technique combined with an iterative method to obtain physically reasonable boundary values for the first-guess profile required in the regularization technique. In the application of this technique to field data, it was established that there is an additional requirement to perform averages in the spectral measurements to reduce noise and allow the solution to converge. The noise-added synthetic data results show a brightness temperature error of $<$0.016% and $<$0.11% when calculated at 300 K between wave numbers 800–1,200 and 2,640–2,800 cm^{-1}, respectively (Wong & Minnett 2016a).

3.2. Infrared Radiation From Clouds

Detecting changes in the downwelling IR irradiance resulting from increases in anthropogenic GHGs is difficult since consistent data sets with long timeframes and exceptionally good calibration are required to produce a significantly detectable signal, expected to be $<$1 W m^{-2} over several decades (Levitus et al, 2012). Seeking indirect evidence of the effects of increasing IR radiation incident at the sea surface through changes in the SST is also very challenging. Ohring et al. (2005) have determined that an accuracy of 0.1 K and a stability of 0.04 K $decade^{-1}$ are required for satellite-derived SST fields to detect climate change signals, and the situation is rendered more challenging by the sampling errors that are introduced by the presence of clouds (Liu et al., 2017; Liu & Minnett, 2016). For in situ measurements, the time series of subsurface temperatures from drifting buoys are perhaps the most promising data set, but these do not have the

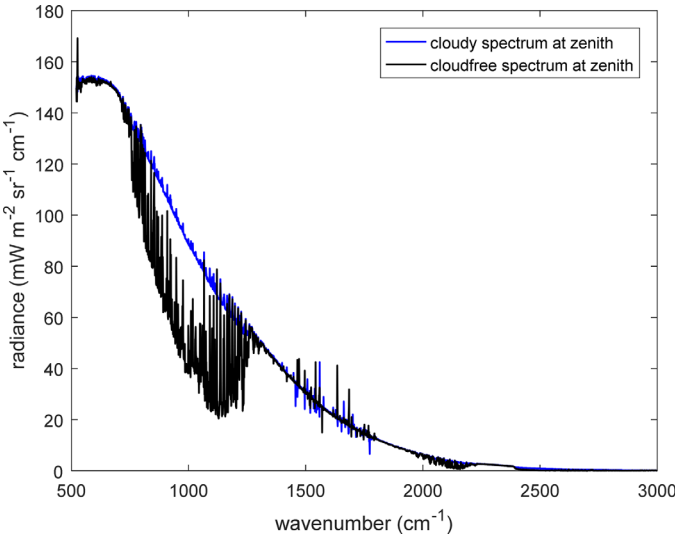

Figure 3. Sample M-AERI spectra measured at zenith under tropical conditions. The black line is a spectrum taken in cloud-free conditions; blue line denotes a spectrum in the presence of low-level clouds.

required accuracy (O'Carroll et al., 2008) and have large sampling errors caused by irregular deployment locations and times, and the subsequent drift of each buoy (Lumpkin et al., 2016). Even though the M-AERIs are likely to be able to meet the accuracy requirements, there are only about two decades of measurements at sporadic locations, which introduce significant sampling errors when seeking the evidence of the effects of increasing IR radiation at the surface. Thus, we have exploited the variability of clouds overhead during sequences of M-AERI measurements as a surrogate for an increase in atmospheric IR emission due to rising levels of GHG. As this is an indirect approach to the problem, there are pros and cons to the technique of using clouds as the IR forcing. This section addresses whether the spectral signature of clouds is representative of the spectral signature of GHGs and if the analyses from cloud forcing is a suitable tool for understanding the effects of increasing concentrations of GHGs.

Under clouds, there is an increase in downwelling IR radiation at the sea surface from the emission from clouds radiating at higher temperatures than of the upper atmosphere in cloud-free conditions. Figure 3 shows the atmospheric spectrum when the M-AERI is measuring radiation at zenith. When no clouds are present overhead (black line), we note the presence of an atmospheric window (where the atmosphere is more transmissive) from ~800 to 1,250 cm^{-1}. When a low cloud is overhead (blue line), the M-AERI senses radiation emitted from the cloud base which occurs at a higher temperature and results in a closure of the atmospheric window and a higher IR emission.

The advantage in using cloud cover as a surrogate of GHG's is the large signal in incoming longwave, LW_{in} (about an increase of 200 W m^{-2}) produced in short time intervals, as compared to a typical forcing of 3.7 W m^{-2} anticipated for a doubling of CO_2 (IPCC, 2014; MacDougall et al., 2017; Ramanathan et al., 1979). This higher signal enables us to detect the response of the curvature of the TSL resulting from increased LW_{in} and therefore provides an approach to address the problem.

An issue that needs to be addressed is the difference in spectral composition between the downwelling IR spectrum due to the presence or absence of clouds and contributions from each GHG. The different spectral compositions of the four main GHGs (H_2O, CO_2, O_3, and CH_4) are shown in Figure 4 calculated using an emission temperature of 300 K, chosen as being a reasonable value for the tropical conditions used in this study. The first spectral difference noted between Figures 3 and 4 is the absence of data for wave numbers <500 cm^{-1} in the M-AERI spectra. In this region, we observe that H_2O has an absorptivity of ~100% (~0% transmittance) while CO_2, O_3, and CH_4 show the reverse (low absorptivity and high transmittance). Changes in atmospheric H_2O would therefore have a minor effect in the downwelling IR spectrum from 0 to 500 cm^{-1}. The field data in this study were taken in the tropics, with a typical relative humidity of 75%. Thus, the absence of data from 0 to 500 cm^{-1} within M-AERI spectra is not of major concern due to the high humidity with relatively small variability, and low transmissivity in the tropical atmosphere.

Other prominent differences in spectral composition are the narrow absorption bands in CO_2, O_3, and CH_4 emission at approximately 520–800 and 2,200–2,400 cm^{-1} for CO_2, 560–880 and 920–1,240 cm^{-1} for O_3, and 1,080–1,490 cm^{-1} for CH_4 where the transmissivity approaches zero implying that the atmosphere is essentially opaque at these wave numbers. H_2O does not contribute to the absorption in these spectral regions as it has a transmissivity approaching unity. This means that in these bands, when an increase in CO_2, O_3, or CH_4 occurs, there will be an increase in absorption and emission of radiation resulting in an increase in the downwelling radiation within these wave number ranges, whereas this effect will not be observed if there is an increase in H_2O. How the spectral features of CO_2, O_3, and CH_4 modify the response of the TSL's gradient compared to increasing clouds or H_2O vapor concentration requires further study, but a thorough assessment would require full radiative modeling through the atmosphere and in the TSL, which is beyond the scope of this paper. Therefore, to address this issue, we perform a simpler analysis by considering atmospheric spectra under a cloudy and clear sky situation simulated by a line-by-line radiative transfer model (LBLRTM; Clough et al., 2005) and assuming only a beam of radiation impinging onto the sea surface from zenith.

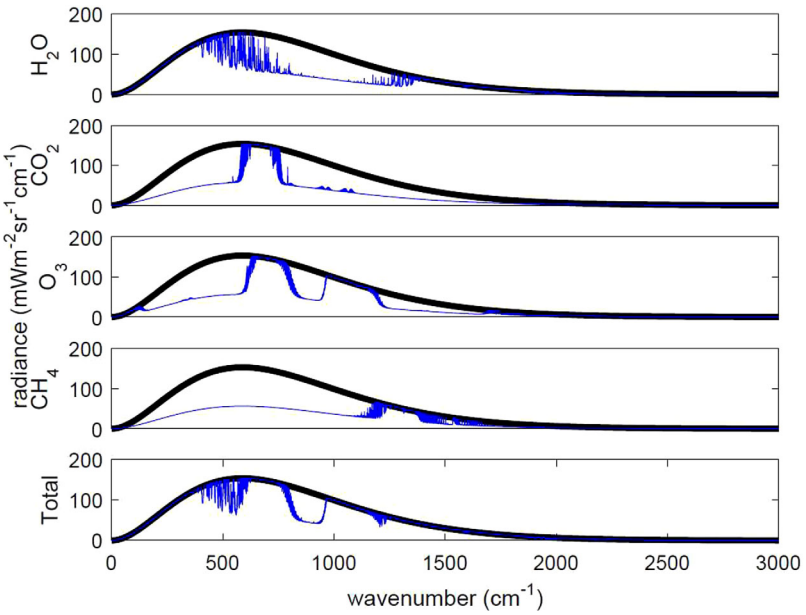

Figure 4. Calculated emission spectra of four different greenhouse gases. The black line shows the spectrum calculated using Planck's function at 300 K. The blue lines show the contributions of selected GHGs at a surface temperature of 300 K. Molecular data are taken from the high-resolution transmission absorption database (HITRAN; Rothman, 2013).

Heating rate profiles were generated using US Standard atmosphere profiles and assuming conditions under (a) clear sky spectrum (1 × CO_2; 356.9 ppm), (b) cloudy sky spectrum, (c) 2 × CO_2 spectrum generated from (a), and (d) 3 × CO_2 spectrum generated from (a). The differences in heating rate profiles are shown in Figure 5 along with the differences in atmospheric spectra.

From Figure 5, we note that the difference between cloudy and clear sky spectra has a much higher magnitude and broader spectral range compared to the difference between a 2 × CO_2 or 3 × CO_2 and clear sky spectra. Clouds generate a radiance difference of up to ∼40 mW m^{-2} sr^{-1} $(cm^{-1})^{-1}$, about 8 times that of the 3 × CO_2 spectrum (∼5 mW m^{-2} sr^{-1} $(cm^{-1})^{-1}$). Thus, we expect to see a much larger change in the heating rates for cloud forcing. The bottom plot of Figure 5 shows that the cloud forcing produces a total difference in absorbed radiation of ∼9 W m^{-2} sr^{-1} at the surface whereas 3 × CO_2 forcing only gives ∼500 mW m^{-2} sr^{-1}. In addition, CO_2 forcing is observed to vary the top 0.01 mm of the TSL while the effect of cloud forcing extends much deeper (to about 0.09 mm). Thus, in comparison with greenhouse gas radiative forcing, cloud forcing amplifies the vertical temperature profile in the TSL resulting in signals that are detectable in M-AERI sea-surface emission spectra.

It is also important to consider the effects of an increase in water vapor due to the warming of the atmosphere through a doubling of CO_2. With Earth's warming, the saturation vapor pressure increases exponentially from the Clausius-Clapeyron equation: $e_s = e_0 \times \exp((L_v/R_v)(T_0^{-1} - T^{-1}))$, where e_s is the saturation vapor pressure at T, e_0 is the vapor pressure at temperature T_0, L_v is the latent heat of vaporization and $R_v = 8.314$ J mol^{-1} K^{-1}. This means that at warmer temperatures, more water vapor can be present in the atmosphere without reaching saturation. Thus, even though climate models introduce a typical forcing of doubling CO_2 concentrations (Ramanathan et al., 1979) in the atmosphere, which is very small compared to cloud forcing, to analyze its effects on global warming, the increase in anthropogenic GHGs would also increase the capacity of the atmosphere to hold more water vapor in the lower troposphere, generating a positive feedback. Our analysis using variations in cloud cover is therefore seen to be a good, but imperfect, tool for studying the consequences of increasing concentrations of GHGs.

4. Data

This section presents the measurements taken at sea during two research cruises in tropical and equatorial conditions used in our research.

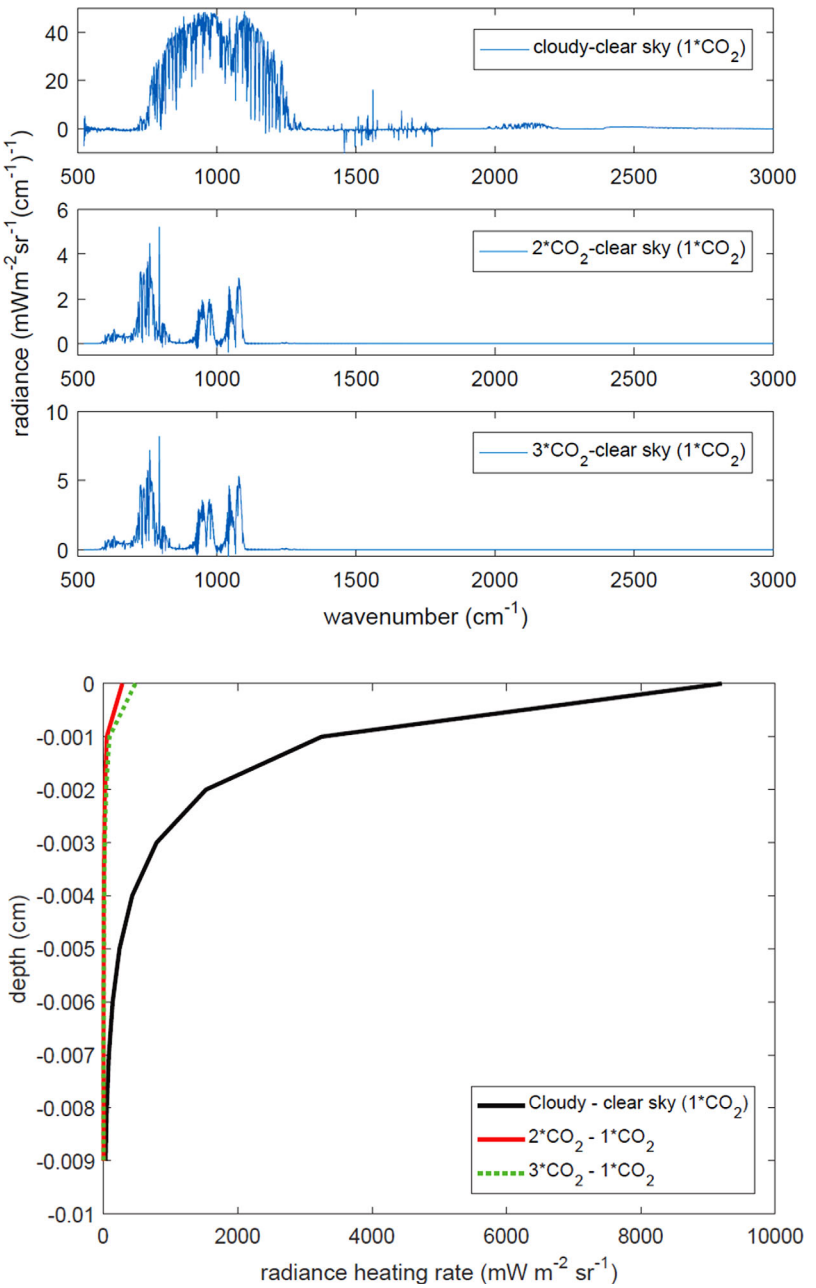

Figure 5. (top) Difference in atmospheric spectra with respect to a 1 × CO_2 (clear sky) atmospheric spectrum. (bottom) Difference in heating rate profiles with respect to a heating rate profile derived from a 1 × CO_2 (clear sky) spectrum. Concentration of CO_2 used is 356.9 ppm.

4.1. Field Data

We use M-AERI measurements from two field programs (NAURU99 and the African Monsoon Multidisciplinary Analyses [AMMA06]) chosen because of the relatively low wind speeds (<10 m s^{-1}), variable cloud cover, and infrequent precipitation. The low wind speeds and precipitation ensure plentiful readings in which there will be no disruption of the TSL by breaking waves or raindrops. A sufficient number of clear sky spectra are important as we rely on these data to determine the spectral emissivity which utilizes the atmospheric absorption features reflected at the sea surface (masked by low-level and midlevel clouds) for its derivation (Hanafin, 2002; Minnett et al., 2001). For our analysis, only nighttime data (20:00–05:00 h local time for NAURU99 and AMMA06, about 2 h after sunset) were used to avoid possible contamination of the higher wave number measurements by reflected and scattered solar radiation.

The Nauru 1999 (NAURU99) was a joint program between the Department of Energy's Atmospheric Radiation Measurement program, the National Oceanic and Atmospheric Administration (NOAA) and the Japan Marine Science and Technology Center (JAMSTEC). It was conducted in the tropical western Pacific Ocean in June and July 1999. An M-AERI installed on the research vessel (RV) *Mirai*, left Yokohama, Japan on 5 June and headed south to Nauru. The Intensive Observation Period (IOP) took place near the island of Nauru from 17 June to 4 July 1999. The IOP was characterized by fair weather with light to moderate winds with air temperatures ranging from 299 to 302 K and SSTs from 301 to 303 K. The wind speed ranged from 0 to 9 m s^{-1} with a relative humidity of 65%–82% and air pressure of 1,008–1,014 hPa.

Measurements taken by the M-AERI during the AMMA 2006 cruise (AMMA06) of the NOAA Ship *Ronald H. Brown* (RHB) took place in the tropical Atlantic Ocean from 28 May to 14 July 2006. AMMA06 was a coordinated international project conducted to improve knowledge and understanding of the West African Monsoon, its variability and impacts. There were two legs to the cruise: Leg 1 was from 28 May to 17 June where the RHB left San Juan, Puerto Rico, heading south-east with majority of the time being spent off West Africa. Leg 2 was from 22 June to 14 July, leaving Recife, Brazil, and returning to Charleston, SC. Measurements from the M-AERI began on 28 May and ended on 14 July 2006. A gap from 17 June to 22 June corresponds to a port call in Recife, Brazil, while other larger time gaps found in M-AERI data were due to instrument failure or periods of bad weather. The skin SST temperature ranged from 295 to 305 K. The ranges of meteorological variables were: air temperatures from 295 to 302 K, air pressures from 1,010 to 1,030 hPa, relative humidity from 50% to 80% with wind speeds from 0 to 20 m s^{-1}.

4.2. Definitions

To analyse the dependences of the retrieved TSL profile on air-sea fluxes, we have extracted and defined variables from the retrieved profiles which will be used in the analyses. These variables are shown in Figure 6.

The longwave variables are defined as follows: (a) LW_{in}, the broadband hemispheric radiance incident at the sea surface from the hemisphere above; (b) LW_{out}, the broadband hemispheric radiance emitted at the sea surface into the hemisphere above; (c) $LW_{in@zenith}$, the integrated spectral irradiance measurements measured at zenith from the M-AERI.

Figure 6 shows that the subskin temperature and depth are defined as the lower boundary of the TSL and below this boundary occurs the isothermal, well-mixed layer. Implicit in Figure 6 is the assumption that the isothermal mixed layer at night extends at least to a depth of 5 m, and that the measurable quantity SST_{5m} is a good representation of $SST_{subskin}$, which is difficult to measure. There are possible effects of residual warming from the diurnal thermocline caused by absorption of solar radiation from the previous day especially during very light wind situations. There are few studies which focus on the erosion of the diurnal thermocline during nighttime conditions as most focus on the daytime response to solar heating. The availability of reliable at-sea in situ measurements of the nighttime temperature structure in the top few meters are rare given the difficulty in obtaining such measurements which require high vertical resolution data taken beyond the influence of the ship. Near-surface measurements thus require instrumentation

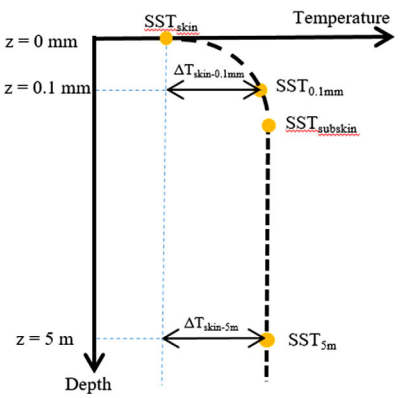

Variable	Meaning
SST_{skin}	Temperature at z ≈ 0 mm; close to the air-sea interface. Coldest temperature in the TSL profile derived from M-AERI measurements.
$SST_{subskin}$	Temperature at lower boundary of the TSL, where the TSL profile transitions to the water below.
$SST_{0.1mm}$	Temperature at the maximum penetration depth of the EM skin layer within wavenumbers 500-3000 cm^{-1}; the depth of 0.1mm is notional. The warmest temperature in the TSL profile derived from M-AERI measurements.
SST_{5m}	Thermosalingraph measurement at z = 5 m.
$\Delta T_{skin-5m}$	Temperature difference between SST_{skin} and SST_{5m}.
$\Delta T_{skin-0.1mm}$	Temperature difference between SST_{skin} and $SST_{0.1mm}$.
$\Delta T_{0.1mm}/\Delta T_{5m}$	Ratio of $\Delta T_{skin-0.1mm}$ to $\Delta T_{skin-5m}$.

Figure 6. Cartoon of the thermal skin layer profile during nighttime conditions with properties and description of the thermal skin layer indicated.

mounted ahead of the ship (Soloviev & Lukas, 1997) or at the top of surface-piercing autonomous vertical profilers (Caldwell et al., 1985; Ward et al., 2004, 2014). Using measurements of an autonomous profiler in the equatorial Pacific, Moum et al. (1989) reported at night "in this region, turbulence appeared to propagate vertically at 5 m h^{-1}, and sometimes persisted past daybreak." Their analysis focused on the density and turbulent kinetic energy structure in the upper ocean, but the generation of an isopycnic surface layer can be presumed to create an isothermal layer. All in situ measurements show the presence of an isothermal layer to 5 m and deeper (in so far as can be determined from published plots) forming soon after sunset and persisting through the night. Thus, to increase the likelihood that there are no temperature differences above 5 m from residual diurnal warming on the previous day, nighttime data have been defined as starting 2 h after sunset (as mentioned in section 4.1; Scanlon et al., 2013; Soloviev & Lukas, 1997; Sutherland et al., 2014, 2016). However, there are cases where the diurnal heating effects persist beyond 2 h after sunset, especially for low wind speed, and in these conditions, additional noise will be introduced into our analysis.

4.3. Surface Heat Fluxes

The incoming IR radiative flux at the surface, $LW_{in@zenith}$, was calculated by integrating the spectral M-AERI's calibrated irradiance measurements at zenith in a narrow beam, with a full angle of 45 mrad, and covering a wave number interval ranging from 500 to 3,000 cm^{-1}. Given the good calibration of the M-AERI, $LW_{in@zenith}$ provides an accurate measurement of the incoming longwave flux as opposed to a hemispheric broadband incident radiation LW_{in} measured using commercially available pyrgeometers which are difficult to calibrate (Miyahara & Aoshima, 2015; Philipona et al., 1998), especially at sea. The units of $LW_{in@zenith}$ are W sr^{-1} m^{-2}. The advantages in using $LW_{in@zenith}$ are further discussed in section 6.1.

The outgoing longwave flux, LW_{out}, is calculated by Stefan-Boltzmann's law, $\epsilon\sigma T^4$, where T is the retrieved SST_{skin}, ϵ is the spectrally averaged surface emissivity, and σ is Stefan-Boltzmann's constant. Turbulent fluxes of sensible (SH) and latent heat (LH) are calculated using the bulk aerodynamic formulae where the exchange coefficients are derived by Kara et al. (2005). SH is calculated from the skin SST values and air temperature values retrieved from the M-AERI where the absolute uncertainty of the values is $<$0.1 K. Similarly, LH is calculated using skin SST and air temperature values from the M-AERI (with a similar uncertainty) using the Bolton formula to obtain the water vapor pressure (Bolton, 1980) from relative humidity measurements from meteorological stations mounted forward on the ship. Relative humidity was measured by Vaisala Humicap^{TM} sensors, which have typical uncertainties of $<$5%. The wind speeds are from anemometers on the ships, R M Young wind monitors with speed and direction accuracies of 0.3 m s^{-1} and 3°; the effects of ship motion have been removed using navigation data, but no correction has been applied for flow distortion caused by the ship. All fluxes are defined negative for an upward flow (heat loss from the ocean to the atmosphere).

5. Results

We present the results of our study in three parts. First, we show that the increased energy in the E-M skin layer that is caused by the absorption of greater incident IR radiation is not immediately returned to the atmosphere through increased turbulent or radiative heat losses. These results are not surprising, but are important in establishing the basis of our interpretation of the behavior of the TSL under conditions of varying incident IR radiation. Then we present evidence of the TSL thickness increasing at lower wind speeds, and finally we argue that the curvature of the vertical temperature profile within the TSL is dependent on the incident IR radiative flux.

5.1. Relationship Between Incoming Radiative Flux and Outgoing Fluxes

To ensure that the hypothesis is well-framed, we need to ensure that the incoming radiative flux, $LW_{in@zenith}$ is decoupled with the immediate changes in the outgoing turbulent and radiative fluxes, LH, SH and LW_{out}. To repeat, the hypothesis we are investigating is to test whether internal adjustment of the TSL in response to changing infrared radiation at the sea surface can provide a mechanism for the retention of heat in the water beneath. Scatterplots of SH and LH versus $LW_{in@zenith}$ (not shown) yielded a coefficient of determination, R^2, of 0.0097 and 0.013 for SH and LH, respectively. The lack of correlation, at least to first order, between SH and LH with $LW_{in@zenith}$ is expected given the different physical processes involved. This

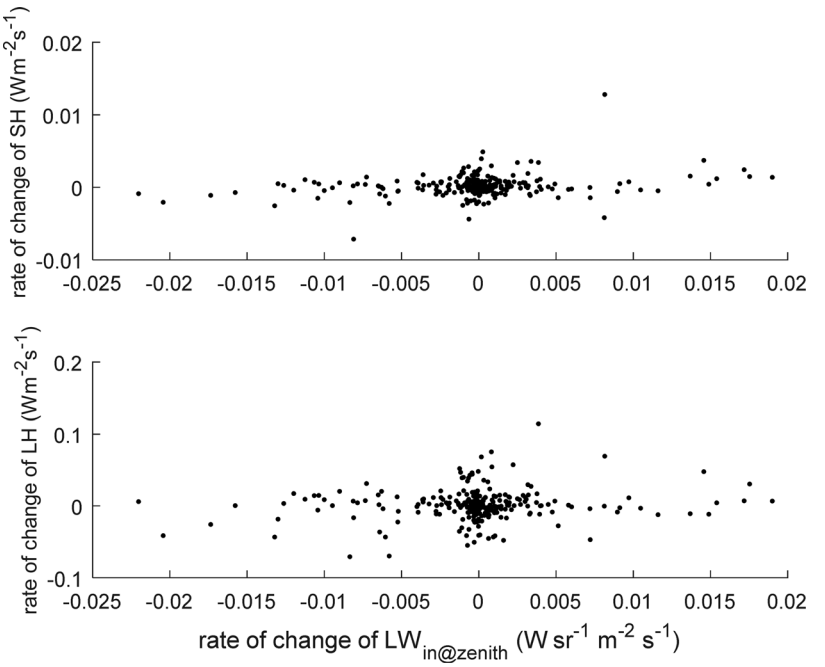

Figure 7. Rate of change of sensible and latent heat fluxes with the rate of change of incident IR radiation at zenith.

indicates that the additional energy from the absorption of increased LW_{in} is not immediately released to the atmosphere through enhanced turbulent heat fluxes.

Because cloud forcing is used as a surrogate to GHG forcing, we also need to ensure that there is no coupling between the effect of clouds and turbulent fluxes, such as increased winds due to the presence of convective clouds resulting in an increase of LH and SH (Jabouille et al., 1996). The rate of change of turbulent fluxes with the rate of change of $LW_{in@zenith}$ is given in Figure 7. For Figure 7, the period for the rate of change calculations are within 1 h intervals. The same analysis was performed for ~10 min intervals with similar results. No correlation is found between these parameters thus indicating the turbulent heat loss does not immediately respond to increased $LW_{in@zenith}$ for our data set.

With respect to LW_{out}, a simple analysis shows that the absorption of increased LW_{in} does not increase the SST_{skin} temperature such that LW_{out} compensates the release of heat back into the atmosphere. For example, assuming an initial SST_{skin} of 300 K which corresponds to LW_{out} of 459 W m^{-2} from Stefan Boltzmann's law, if the LW_{in} increases by 20 W m^{-2} and assuming all this energy is to be released back into the atmosphere through LW_{out}, this implies that SST_{skin} would increase by ~3 K, which is not observed. LW_{out} therefore does not respond immediately to increase in the incident IR radiation.

The results therefore rule out the immediate release of heat from the absorption of the cloud IR irradiance back into the atmosphere through processes such as evaporation and increased IR emission. There is thus an increase in the rate of heat production in the skin layer, while the heat sink at the top of the skin layer remains essentially unchanged. Figure 8 illustrates the fluxes at the surface and the heat flow through the TSL at low wind speeds with and without the presence of clouds. The flux values are averages from both research cruises. Figure 8 shows that since the outgoing fluxes of LW_{out}, LH and SH do not immediately change with increased LW_{in}, the additional heat from the increased radiative forcing has "replaced" part of the heat flux input from the mixed layer below resulting in the contribution of heat from the mixed layer to be reduced. Therefore, less heat is supplied from the mixed layer to the base of the TSL. The next question we address is how does the TSL respond to the increased heating in the EM skin layer?

5.2. Wind Speed Dependence

In this section, we establish the relationships between retrieved temperature differences across the TSL, $\Delta T_{skin\text{-}5m}$, $\Delta T_{skin\text{-}0.1mm}$ and $\Delta T_{0.1mm}/\Delta T_{5m}$ with wind speed, U_{10}. U_{10} is derived assuming neutrally stable atmospheric conditions.

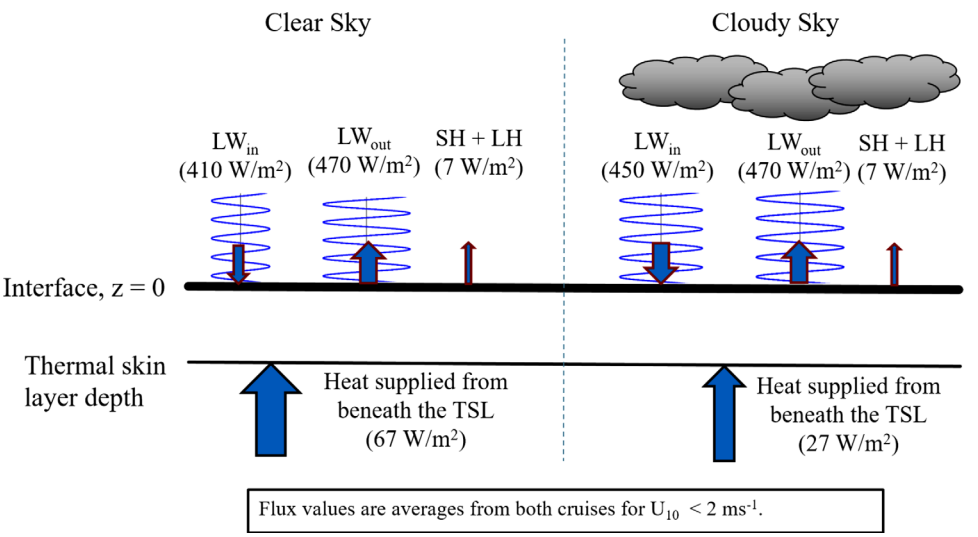

Figure 8. Time-averaged heat balance of the TSL with and without clouds. These are average values for both cruises used in this study.

Figure 9 shows the dependence of $\Delta T_{skin\text{-}5m}$ and $\Delta T_{skin\text{-}0.1mm}$ with U_{10}. The magenta triangle line shows the Donlon et al. (2002) parameterization of $\Delta T_{skin\text{-}5m}$ against U_{10} based on measurements from six research cruises from multiple investigators in which the skin temperature was defined as the temperature measured by sea-going radiometers of several different designs, and the temperature at ~5 m depths were measured by thermosalinographs on the ships. Only nighttime data were used to avoid the confusing signal from diurnal heating that is strongly wind speed dependent, especially at low winds (Minnett, 2003). The line with the green triangles shows the Minnett et al. (2011) parameterization of $\Delta T_{skin\text{-}5cm}$ against U_{10} based on field measurements from a research cruise off New Zealand with $\Delta T_{skin\text{-}5cm}$ defined to be the temperature difference between the ocean's skin temperature measured by an M-AERI and the temperature at 5 cm depth measured by a thermometer on a small, surface-following float tethered close to the footprint on the sea surface of the M-AERI field of view. Measurements taken during both day and night were used. A least squares approximation to our field data, binned to every 1 m s^{-1}, using the same form of the equation Donlon et al. (2002) and Minnett et al. (2011) used for their parameterizations: $\Delta T = A + B \times \exp(-U_{10}/C)$, was performed and is denoted by the blue and red lines. The mean and ±1 standard deviation are represented by the blue and red triangles and error bars in Figure 9.

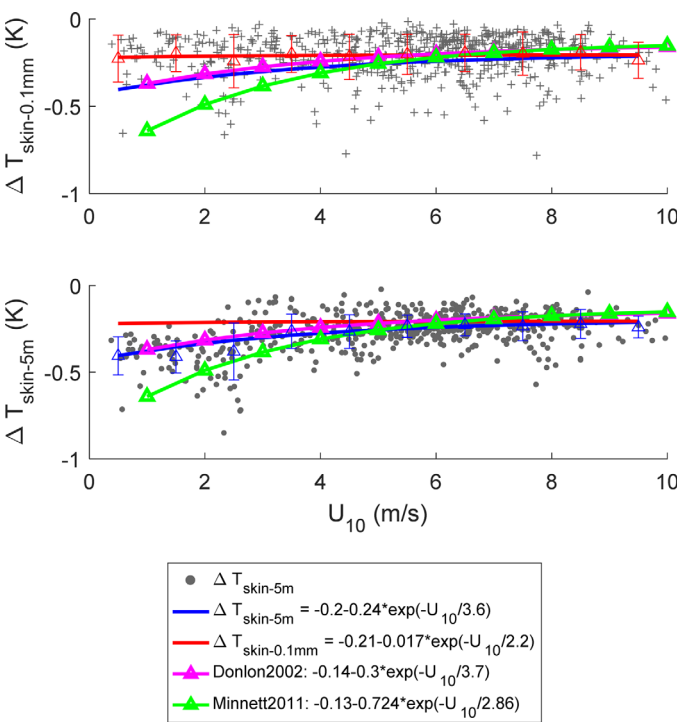

Figure 9. Scatterplot of (top) $\Delta T_{skin\text{-}0.1mm}$ (grey +) and (bottom) $\Delta T_{skin\text{-}5m}$ (solid grey dots) versus U_{10}. Red line represents least squares fit to the mean values (red triangles) of $\Delta T_{skin\text{-}0.1mm}$. Blue line represents least squares fit to the mean values (blue triangles) of $\Delta T_{skin\text{-}5m}$. Both averages are calculated at every 1 m s^{-1} interval and the blue and red error bars corresponds to ±1 standard deviation. Magenta triangle line denotes the Donlon et al. (2002) parameterization while green triangle line denotes the Minnett et al. (2011) parameterization.

Comparing first the coefficient A, which signifies the asymptotic value when U_{10} is large, the values are similar for both $\Delta T_{skin\text{-}5m}$ and $\Delta T_{skin\text{-}0.1mm}$ meaning that at high wind speeds, both $\Delta T_{skin\text{-}5m}$ and $\Delta T_{skin\text{-}0.1m}$ tend to −0.2 K and indicates there is close agreement between $SST_{0.1mm}$ and SST_{5m}. This implies that at high winds, the temperature profile is essentially isothermal between depths of 0.1 mm to 5 m thereby suggesting that the TSL profile is within the deepest emission depth of the EM skin layer of ~0.1 mm (Figure 1) and $SST_{0.1mm}$ is measuring the value of $SST_{subskin}$. This result is expected under higher wind conditions as the wind driven shear erodes the viscous skin layer and the TSL resulting in the mean skin layer being thinner (e.g., Saunders, 1967; Soloviev & Schlüssel, 1994) and we expect an isothermal mixed layer beneath the TSL, i.e. no solar heating, since our data are confined to nighttime conditions.

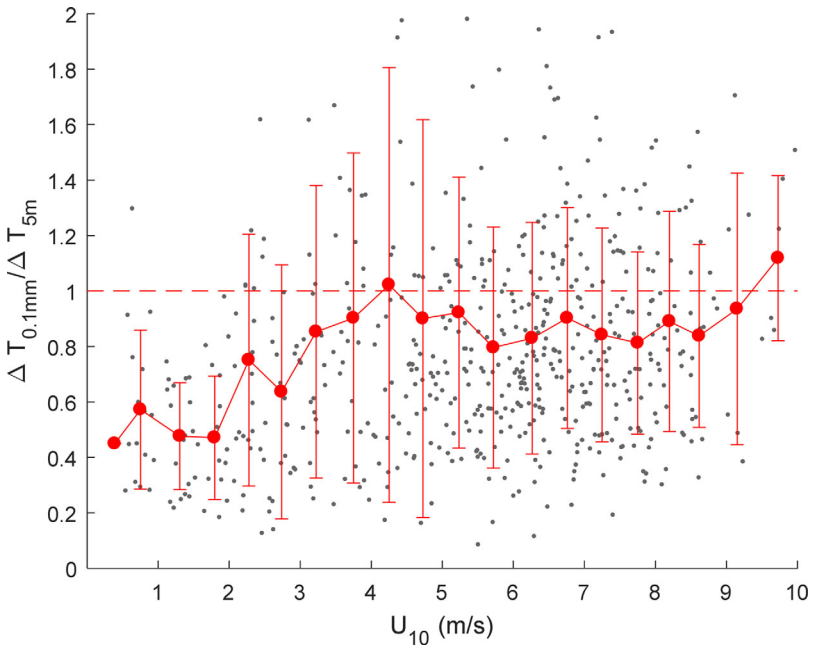

Figure 10. Plot of $\Delta T_{0.1mm}/\Delta T_{5m}$ versus U_{10} (grey dots). Red dots represent $\Delta T_{0.1mm}/\Delta T_{5m}$ average values binned at every 0.5 m s^{-1}. Red dotted line represents $\Delta T_{0.1mm}/\Delta T_{5m} = 1$.

Donlon et al. (2002) suggested that coefficient C is indicative of a threshold value that signifies the transition from free convective and molecular heat transfer processes (at lower U_{10}) to wind-induced shear-driven turbulent heat transfer (at higher U_{10}). Donlon et al. (2002) mentioned that their value of 3.7 m s^{-1} "marks the onset of ubiquitous small waves on the sea surface" and noted the stronger wind speed dependence of ΔT at $U_{10} < 2$ m s^{-1} which is similarly seen in our data of $\Delta T_{skin\text{-}5m}$. Our C value of 3.5 m s^{-1} for $\Delta T_{skin\text{-}5m}$ is closer to the Donlon et al. (2002) C value than that of Minnett et al. (2011). This may be due to the latitudinal variations between data sets as that of Minnett et al. (2011) was taken at higher southern latitudes during the end of the summer months (March–April 2004), whereas that of Donlon et al. (2002) is derived from wider geographical and temporal ranges.

The parameterized $\Delta T_{skin\text{-}0.1mm}$ (red line) shows that the absolute temperature difference between the skin and at a depth of 0.1 mm does not change with wind speed. It is interesting to note the increased deviation between $\Delta T_{skin\text{-}0.1mm}$ and $\Delta T_{skin\text{-}5m}$ as the winds decrease (from about $U_{10} < 3.5$ m s^{-1}). This suggests that the TSL profile has extended deeper than the deepest emission depth of the EM skin layer of ~0.1 mm within wave numbers 500–3,000 cm^{-1} and that $SST_{0.1mm}$ is not measuring $SST_{subskin}$, thereby limiting the retrieval of $SST_{subskin}$ from the M-AERI spectra.

This issue is illustrated further by plotting $\Delta T_{0.1mm}/\Delta T_{5m}$ with U_{10} (Figure 10). $\Delta T_{0.1mm}/\Delta T_{5m}$ represents the fraction of the total temperature change across the TSL that is sampled by the M-AERI profile retrievals. A smaller ratio means a larger difference between $SST_{0.1mm}$ and SST_{5m} which implies that more of the vertical temperature gradient of the TSL lies below the emission depth. $\Delta T_{skin\text{-}0.1mm}$ deviates from $\Delta T_{skin\text{-}5m}$ at ~3.5 m s^{-1} and approaches a value of ~0.5 below ~2 m s^{-1}. This suggests that as winds increase from 2 to 3.5 m s^{-1}, wind effects start eroding and thinning the TSL through increased levels of turbulence below. For wind speeds below 2 m s^{-1}, the TSL is thicker. This also shows that in order to remove the effect of winds for our analysis, there is a need to focus on data with wind speeds of less than 2 m s^{-1}.

Moreover, analysis of the net flux, Q, with $LW_{in@zenith}$ (Figure 11) shows that below 2 m s^{-1}, Q is primarily dependent on $LW_{in@zenith}$ and not well correlated with the turbulent fluxes. As the winds increase, the net heat flux out of the ocean correlates with the turbulent fluxes and the effect of winds as turbulent fluxes play a larger role in the interfacial heat loss. This is expected as the magnitude of the turbulent fluxes is dependent on wind speed. Thus, to focus our analysis to the response of the TSL to radiative effects, we analyze data with $U_{10} < 2$ m s^{-1}. This reduces the effects of wind-driven shear and allows the focus to be on effects due to interfacial fluxes and molecular heat transfer processes.

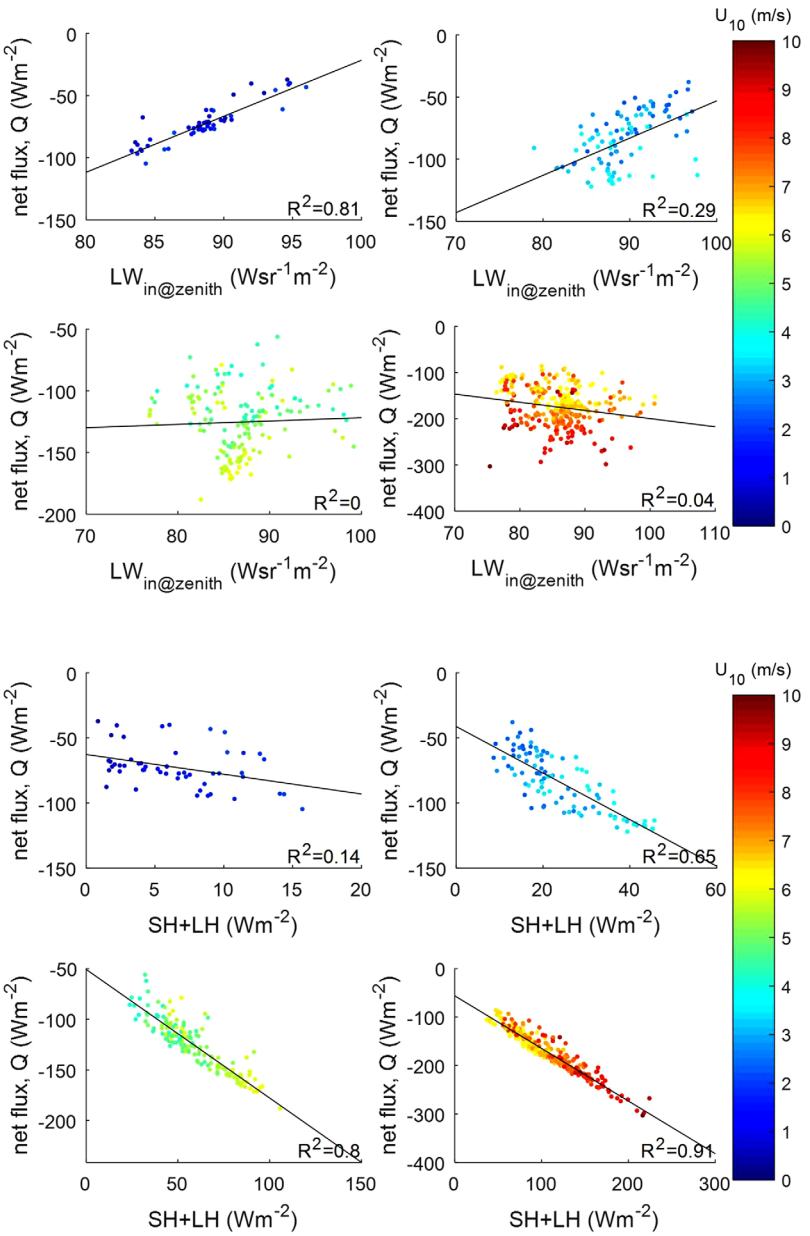

Figure 11. (top four plots) Plot of net flux, Q, against $LW_{in@zenith}$ segregated into wind speed regimes of <2, 2–4, 4–6, and 6–10 m s^{-1}. (bottom four plots) Plot of net flux against sensible heat (SH) and latent heat (LH) fluxes segregated into wind speed regimes of <2, 2–4, 4–6, and 6–10 m s^{-1}. Black lines represent least squares fit to the scatterplots.

It is unfortunate that $SST_{0.1mm}$ does not fully capture the TSL temperature difference at low winds. However, the agreement between $\Delta T_{0.1mm}$ and ΔT_{5m} at high winds provides evidence to support existing TSL models that the thickness of the TSL is inversely proportional to wind speed (e.g., Fairall et al., 1996; Saunders, 1967; Soloviev & Schlüssel, 1994) and indicates that the retrieved $\Delta T_{skin\text{-}0.1mm}$ are accurate. Because our retrievals are limited by the emission depth of the EM skin layer thereby restricting the retrievals to the top ~0.1 mm, the divergence between $\Delta T_{skin\text{-}0.1mm}$ and $\Delta T_{skin\text{-}5m}$ at low winds tells us that the subskin temperature occurs beyond a depth of 0.1 mm.

5.3. Surface Fluxes

In this section, we focus on data with $U_{10} < 2$ m s^{-1} where it has been established that Q is dominated by radiative fluxes, reducing the effects of turbulent fluxes.

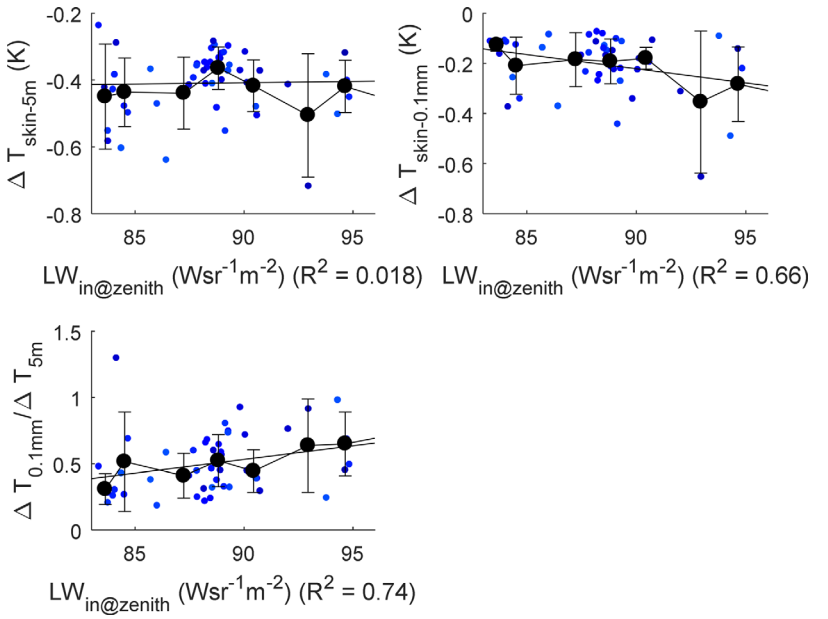

Figure 12. (top left) $\Delta T_{skin\text{-}5m}$ versus $LW_{in@zenith}$ at winds <2 m s^{-1}. (top right) $\Delta T_{skin\text{-}0.1mm}$ versus $LW_{in@zenith}$ at winds <2 m s^{-1}. (bottom left) $\Delta T_{0.1mm}/\Delta T_{5m}$ versus $LW_{in@zenith}$ at winds <2 m s^{-1}. Blue dots show the scatter. Solid black dots represent points binned every 2 W sr^{-1} m^{-2} of $LW_{in@zenith}$ with ± 1 standard deviation. Black solid lines denote the regressed line to the solid black dots.

As established above, the turbulent fluxes are independent of the radiative fluxes and no coupling was found between wind speed variability due, for example, to convective clouds and the turbulent fluxes, at least over averaging periods of a few minutes to an hour. We analyze the dependence of TSL properties on $LW_{in@zenith}$. The first conclusion from Figure 12 is the lack of correlation between $\Delta T_{skin\text{-}5m}$ with $LW_{in@zenith}$ (left top plot) for both cruises. This means that the changes in radiative fluxes do not affect the total temperature difference across the TSL (SST_{skin}-$SST_{subskin}$). Our result is further supported by Donlon and Robinson (1997) who did not find any dependence between the amount of cloud cover with the temperature difference between the bulk (measured by a SeaBird thermosalinograph at 5.5 m) and skin sea-surface temperature measured radiometrically.

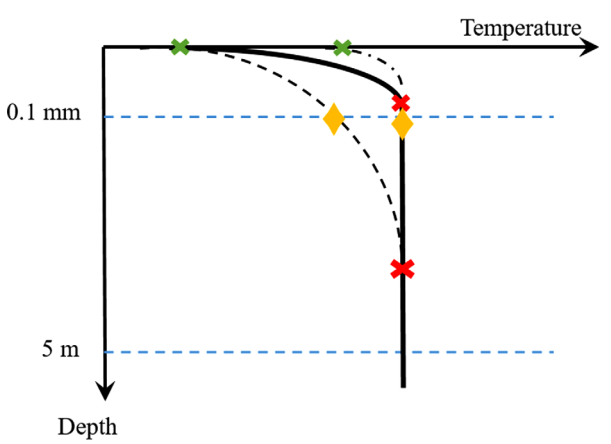

Figure 13. Cartoon of TSL profile under nighttime conditions. Solid black line represents TSL profile under high incoming longwave radiation at low winds (<2 m s^{-1}). Dashed black line represents TSL profile under low incoming longwave radiation at low winds (<2 m s^{-1}). Dash-dotted line represents TSL profile under high winds (>2 m s^{-1}). Yellow star denotes retrieved temperature at 0.1 mm, $SST_{0.1mm}$. Red cross denotes subskin temperature, $SST_{subskin}$. Green stars denote skin temperature, SST_{skin}. The vertical scale is nonlinear.

The top right and bottom left plots of Figure 12 show significant correlations (using a *t* test at a 5% significance level) between $\Delta T_{skin\text{-}0.1mm}$ and $\Delta T_{0.1mm}/\Delta T_{5m}$ with $LW_{in@zenith}$. It is observed that as $LW_{in@zenith}$ increases, $\Delta T_{skin\text{-}0.1mm}$ becomes more negative while $\Delta T_{0.1mm}/\Delta T_{5m}$ increases to approach unity. This result, together with the independence found with $\Delta T_{skin\text{-}5m}$ indicates that there is an adjustment of the curvature of the TSL rather than variations in the temperature difference due to increased longwave radiation from cloud closing the atmospheric window.

Figure 13 illustrates our findings of the response of the TSL profile to increased cloud IR radiative forcing. From the results above, we expect the TSL profile curvature adjusts as the incident IR radiation increases—from the dashed black line to the solid black line in Figure 13. This curvature change agrees with our observations: $\Delta T_{skin\text{-}0.1mm}$ increases, $\Delta T_{skin\text{-}0.1mm}$ approaches $\Delta T_{skin\text{-}5m}$, and there is no change in $\Delta T_{skin\text{-}5m}$. Thus, we interpret our results to indicate that as $LW_{in@zenith}$ increases, the TSL profile varies from a lower to higher gradient near the interface and higher to lower gradient at subskin depths. The adjustment of the TSL profile to a smaller gradient at subskin depths implies that the upward transfer of heat from beneath the TSL

decreases. This finding agrees with our analysis of the independence found between the outgoing fluxes with the incoming flux (section 5a). Figure 13 further shows the situation with higher winds, >2 m/s (dash-dotted line), where the winds have led to the erosion of the TSL resulting in a thinner TSL with a smaller temperature difference thereby allowing $SST_{subskin}$ to be retrieved from the measured spectra as the subskin depth occurs within 0.1 mm of the surface. As opposed to a thicker TSL at low winds (solid and dashed line) which results in the discrepancy in our retrieved $SST_{0.1mm}$ with the measured SST_{5m}.

The curvature adjustment of the temperature in the TSL shows that the additional heat due to absorption of the increased $LW_{in@zenith}$ has modified the TSL profile to reduce the transfer of heat from the mixed layer to the atmosphere. This modification, therefore, provides an explanation for the immediate indirect heating of the ocean even though the increased $LW_{in@zenith}$ is not absorbed throughout the upper few meters of the water column. Thus the heat (which is a product of the absorption of solar radiation during the previous days) within the uppermost few meters of the ocean is unable to escape into the atmosphere, resulting in the retention of heat in the upper ocean.

6. Discussion

The physical processes within and around the skin layers on the aqueous side of the air-sea interface are complex, and occur on a wide range of temporal and spatial scales, some of which are revealed by images taken by IR cameras that show thermal structure in the E-M skin layer (e.g., Jessup et al., 1997; Veron et al., 2011). However, technology does not currently exist to probe the full 3-D structure of the near-surface variability and its dependence on various forcing processes. Here we exploit the spectral measurements of a very well-calibrated IR spectroradiometer, the M-AERI, to study the vertical characteristics of the TSL. To obtain accurate measurements with a sufficiently high signal-to-noise ratio (~5,400 to ~3,200) at the high emitting temperatures of the surface of the topical ocean, with lower values at higher wave numbers, Minnett et al. (2001) require averaging of interferograms that are taken at 1 Hz. The data used here are averages over 46 s for the sea-view. The field of view of the M-AERI at the sea surface is ~1 m^2. At typical speeds of the research ships, the field of view is swept along a path on the sea surface of up to several hundred m. Thus, the measurements analyzed here are time and spatial means that do not resolve the smaller and faster variability in the TSL.

6.1. Incident IR Radiation Measurements

Measurements of the incoming IR radiation were taken from the ships using Eppley Labs Precision Infrared Radiometers (PIRs) mounted on gimbals to reduce the effects of ship motion. PIRs are simple instruments and difficult to calibrate. Even though the PIRs measure the hemispheric, broadband (wavelength range ~4 to ~50 μm) incident radiation is an appropriate parameter for this study, we found that the measurements were too noisy to reveal the dependences. The M-AERI is a well-calibrated instrument and each measurement cycle included spectral measurements at zenith: integrating the spectra provides a measure of the normally incident IR radiation at the surface. Such measurements are used here to represent the changes in the incident IR radiation caused by the presence of clouds overhead.

6.2. Influence of Solar Radiation

The analysis of the TSL with the interfacial radiative fluxes has shown how the absorption of longwave radiation modifies the TSL profile resulting in heat beneath the TSL being retained. The deepest temperatures derived from the M-AERIs are derived from the part of the spectra with the deepest emission depth (Figure 1) at wave numbers of ~2,600 cm^{-1}, wavelengths of ~3.8 μm, where there is significant contamination of the signal by solar radiation reflected at the surface during the day. Thus, our analysis was limited to nighttime measurements, but the physics of the response of the TSL to changes in IR radiation will be the same during the day. However, during the day, the TSL is also influenced by the insolation. Assuming still waters, the heat beneath the TSL is largely a product of the absorption of solar radiation during the day given the penetration depth of solar radiation occurs at meter scales (Lee et al., 2013).

The influence of solar radiation on the TSL can be shown to be small through analysis of the absorptivity of solar radiation in the upper 10 mm of the ocean. The decay of solar irradiance can be calculated from equation (4) (Paulson & Simpson, 1977) to a depth of 10 mm assuming normally incident solar radiation of 1,000 W m^{-2}.

$$SR(-z) = SR(0)\sum_{i=1}^{9} a_i e^{-\beta_i(-z)} \quad (4)$$

The coefficients a_i are the weights corresponding to the spectrally distributed absorption coefficients, β_i, obtained from ibid. $SR(0)$ is the solar radiation at z = 0 m, while $SR(-z)$ is the solar radiation at depth –z from the water surface. Assuming the clearest Jerlov water type I (Jerlov, 1968) and with a tropical sun overhead, the amount of solar radiation absorbed within the upper 0.01 mm was calculated to be 4.9 W m^{-2} (0.049%). The total absorbed solar radiation increases quasi-exponentially with depth with 37 W m^{-2} (3.7%), 132 W m^{-2} (13.2%), and 261 W m^{-2} (26.1%) of solar radiation absorbed at a depth of 0.1 mm, 1 mm, and 1 cm, respectively. As our focus is on the top 0.1 mm from the sea surface, the absorbed solar radiation 37 W m^{-2} in these conditions are therefore an order of magnitude smaller than the energy from atmospheric IR emission (~400 W m^{-2}) absorbed in a similar depth. For nonzero solar zenith angles, the ratio is yet smaller.

6.3. Distribution of Wind Speed

It was found that our analysis needed to be constrained to low winds of less than 2 m s^{-1} to observe significant correlations between the properties of the TSL and radiative fluxes given the limitations of the data and instruments currently available. Above this threshold, wind shear erodes the viscous sublayer which in turn causes the TSL to be thinner, and the ratio of $\Delta T_{0.1mm}/\Delta T_{5m}$ becomes insensitive to wind speed.

Despite imposing a wind speed threshold of 2 m s^{-1} in our study, the physics underlying the modification of the TSL with the absorption of incoming IR radiation will be applicable at winds >2 m s^{-1}. As the signal we seek between the downwelling IR radiation and the TSL is very small, and because of the limitations of current technological capabilities we had to limit the data to very low winds as this gave us a workable TSL signal to establish significant correlations. The limitation in wind speed does not mean that our findings are also limited to such conditions. Although the stronger winds will increase the turbulent transfer of heat to the atmosphere and will thin the TSL (Figure 10), we expect the response of the TSL to changes in incoming IR radiation to be as indicated by our findings. Breaking waves would disrupt the TSL at wind speeds of >~7 m s^{-1}. However, Jessup et al. (1997) showed the TSL reestablishing itself in the wakes of breaking waves in the open ocean through analysis of video and IR images, which means the TSL will modify almost immediately following wave breaking. The recovery times of the TSL are less than 1 s and these results were supported by laboratory measurements. Microscale wave breaking can occur at lower wind speeds, but again, the recovery time of the TSL is very short. Thus, even under breaking wave conditions, the spatial mean TSL is almost always present and will behave as indicated by our findings.

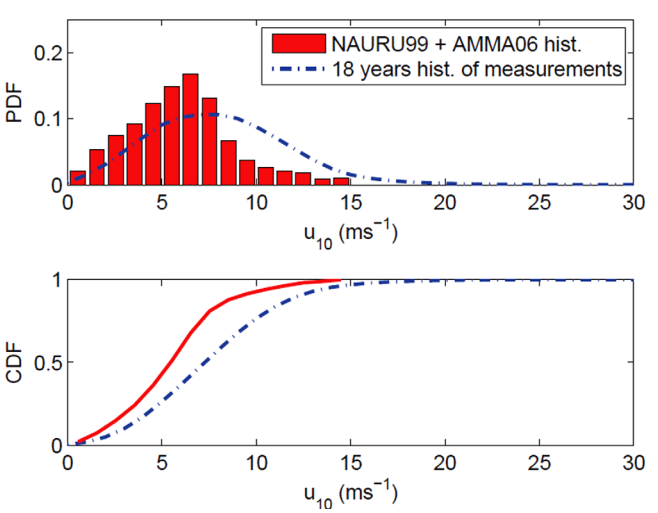

Figure 14. (top) The probability distribution function and (bottom) cumulative distribution function for wind speed data collected from NAURU 1999 and AMMA 2006 and 18 years' histogram of measurements over the entire ocean constructed using Special Sensing Microwave Imager (SSM/I) data version 6. SSM/I wind speed distributions are obtained from Woods et al. (2014).

We considered a wind speed threshold of 7 m s^{-1} and analyzed 18 years of wind speed data over the entire ocean, constructed from the Special Sensing Microwave Imager (SSM/I) data version 6 from 1 January 1988 through 31 December 2006 (Figure 14). The probability distribution function (PDF) and cumulative distribution function (CDF) are obtained from Woods et al. (2014). Figure 14 also shows the combined wind speed for NAURU99 and AMMA06 during the night and day. The percentages calculated show that the majority of winds for our cruise data (81.04%) occur below 7 m s^{-1}, and almost half of the global ocean wind speed distribution (47.13%) is included. Furthermore, a large fraction of wind speeds below 7 m s^{-1} occurs within the equatorial and midlatitude regions (Woods et al., 2014). Our findings on the response of the TSL to increasing IR radiation are therefore representative of the equatorial and midlatitude regions which comprise much of the area of World's Oceans.

7. Conclusions

In summary, we analyzed measurements from two cruises in the tropics held during the summer months and through the analysis of nighttime data with winds less than 10 m s^{-1}, confirmed that the turbulent fluxes (LH and SH) are independent of $LW_{in@zenith}$ and no

significant dependence was found between cloud IR radiative effects and the turbulent fluxes on the spatial and temporal scales of our spectral measurements. Neither was a significant dependence found between LW_{out} and $LW_{in@zenith}$. Establishing these independences is important because it allows us to focus our analysis on the radiative fluxes and supports our hypothesis of the properties of the TSL influencing the heat flow at the interface as it indicates the heat from the absorbed additional IR radiation is not immediately returned to the atmosphere through the upward fluxes of LH, SH, and LW_{out}. Our results also provide initial evidence of the mechanism for increased heat storage in the upper ocean resulting, indirectly, from the absorption of increased IR radiation in the EM skin layer. Since there is no immediate, observable increase in surface heat loss associated with increased absorption of incoming IR radiation from the atmosphere, there is therefore an increase of heat available within the TSL to supply energy for the surface heat losses. It is also not possible for the additional energy in the TSL to be conducted into the bulk of the ocean (i.e., beneath the viscous skin layer) as that would require conduction up a mean temperature gradient in the TSL.

Cloud IR radiative effects were used as a surrogate of the slow increase in downwelling IR radiation on the ocean's surface caused by increasing levels of GHGs. Cloud IR radiative effects were used because of the much larger downwelling IR radiation signal within short time scales (as opposed to attempting to analyze the slow and small GHG signal) which allows the problem to be tractable. However, the spectral emission varies for different atmospheric gases and the absorption coefficients of water also vary with wavelength. Thus, it was necessary to assess whether the downwelling radiative effects on the TSL would be the same under cloud IR radiation and that from GHGs. As discussed in section 3.2, heating rate profiles simulated under different atmospheric gas emission scenarios indicated that cloud cover is an adequate tool for this study as the heating rate profiles of cloud forcing and GHGs are similar. The major difference is the greater magnitudes of the heating rate profiles of cloud forcing as the signal is so much larger; this works to our advantage in addressing the problem at hand.

The additional energy generated from the absorption of IR radiation has been shown to support the change in the TSL temperature gradient. Our results indicate the mean curvature of the TSL has adjusted such that the gradient at the bottom boundary of the TSL adjusts from a higher to lower gradient. This was established through the lack of correlation between $LW_{in@zenith}$ with $\Delta T_{skin\text{-}5m}$ and LW_{out} indicating that the absorption of $LW_{in@zenith}$ is independent of $\Delta T_{skin\text{-}subskin}$ and the correlation observed between $LW_{in@zenith}$ with $\Delta T_{0.1mm}$ and $\Delta T_{0.1mm}/\Delta T_{5m}$ which illustrates that more of the TSL profile exists within the EM skin layer's emission depth of ~0.1 mm as $LW_{in@zenith}$ increases.

Our findings provide an explanation of the mechanism for retaining upper ocean heat content as the incident IR radiation increases. The absorption of increased longwave has been deduced to compress vertically the curvature of the TSL, with a higher gradient forming close to the interface and a lower gradient at subskin depths. The smaller vertical gradient at subskin depths impedes the transfer of heat from the mixed layer into the TSL. Because the heat sink at the interface does not change measurably on the scales of our individual measurements, this means that less heat from the mixed layer contributes to the loss of heat at the interface. This analysis was based on the immediate changes of the TSL to the heat fluxes due to the instantaneous response of the TSL. Greater downwelling infrared forcing would alter the upper ocean heat budget by adjusting the TSL such that more heat beneath the TSL, resulting from the absorption of solar radiation, is retained. This thus provides an explanation for the indirect heating of the ocean by increasing levels of incident infrared radiation and the observed increase in upper ocean heat content.

Attempts to relate directly the curvature of vertical temperature gradient in the TSL and EM skin layer, as developed by Wong and Minnett (2016a, 2016b), to changes in the incident IR radiation did not produce a convincing dependence, at least on the time scales of our measurements. Revealing such a relationship will require more sensitive instruments than are currently available.

Acknowledgments

This study was supported in part by a grant from the NASA Physical Oceanography Program. The Captains, officers, crews, and Chief Scientists of the R/V *Mirai* and NOAA Ship *Ronald H Brown* are thanked for their support in the field. We also thank M. Szczodrak for her help in running the LBLRTM and advice on the processing of the cruise data. Supporting information for the generation of the figures in this paper is available at https://doi.org/10.17604/M6T66Z. For the full data set, please contact the authors.

References

Bertie, J. E., & Lan, Z. (1996). Infrared intensities of liquids XX: The intensity of the OH stretching band of liquid water revisited, and the best current values of the optical constants of H_2O(l) at 25°C between 15,000 and 1 cm^{-1}. *Applied Spectroscopy*, *50*(8), 1047–1057.

Bigg, G. R., Jickells, T. D., Liss, P. S., & Osborn, T. J. (2003). The role of the oceans in climate. *International Journal of Climatology*, *23*(10), 1127–1159.

Bolton, D. (1980). The computation of equivalent potential temperature. *Monthly Weather Review*, *108*, 1046–1053.

Caldwell, D. R., Dillon, T. M., & Moum, J. N. (1985). The rapid-sampling vertical profiler: An evaluation. *Journal of Atmospheric and Oceanic Technology*, *2*(4), 615–625.
Clough, S. A., Shephard, M. W., Mlawer, E. J., Delamere, J. S., Iacono, M. J., Cady-Pereira, K., et al. (2005). Atmospheric radiative transfer modeling: A summary of the AER codes. *Journal of Quantitative Spectroscopy and Radiative Transfer*, *91*, 233–244.
Donlon, C., Minnett, P., Gentemann, C., Nightingale, T. J., Barton, I. J., Ward, B., et al. (2002). Toward improved validation of satellite sea surface skin temperature measurements for climate research. *Journal of Climate*, *15*, 353–369.
Donlon, C., & Robinson, I. (1997). Observations of the oceanic thermal skin in the Atlantic Ocean. *Journal of Geophysical Research*, *102*(C8), 18585–18606.
Eyre, J. R. (1987). On systematic errors in satellite sounding products and their climatological mean values. *Quarterly Journal of the Royal Meteorological Society*, *113*, 279–292.
Fairall, C. W., Bradley, E. F., Godfrey, J. S., Wick, G. A., Edson, J. B., & Young, G. S. (1996). Cool-skin and warm-layer effects on sea surface temperature. *Journal of Geophysical Research*, *101*(C1), 1295–1308.
Gentemann, C., & Minnett, P. J. (2008). Radiometric measurements of ocean surface thermal variability. *Journal of Geophysical Research*, *113*, C08017. https://doi.org/10.1029/2007JC004540
Hanafin, J. A. (2002). *On sea surface properties and characteristics in the infrared* (PhD thesis). Coral Gables, FL: University of Miami.
IPCC. (2014). In C. B. Field et al. (Eds.), *Climate change 2014: Impacts, adaptation, and vulnerability. Part A: Global and sectoral aspects. Contribution of Working Group II to the fifth assessment report of the Intergovernmental Panel on Climate Change*. Cambridge, UK: Cambridge University Press.
Jabouille, P., Redelsperger, J. L., & Lafore, J. P. (1996). Modification of surface fluxes by atmospheric convection in the TOGA COARE region. *Monthly Weather Review*, *124*(5), 816–837.
Jerlov, N. G. (1968). *Optical oceanography*. Amsterdam, the Netherlands: Elsevier.
Jessup, A., Zappa, C., Loewen, M., & Hesany, V. (1997). Infrared remote sensing of breaking waves. *Nature*, *385*, 52–55.
Kara, A. B., Hurlburt, H. E., & Wallcraft, A. J. (2005). Stability-dependent exchange coefficients for air sea fluxes. *Journal of Atmospheric and Oceanic Technology*, *22*, 1080–1094.
Katsaros, K. B., Liu, W. T., Businger, J. A., & Tillman, J. E. (1977). Heat transport and thermal structure in the interfacial boundary layer measured in an open tank of water in turbulent free convection. *Journal of Fluid Mechanics*, *83*, 311–335.
Khundzhua, G. G., & Andreyev, Y. G. (1974). An experimental study of heat exchange between the ocean and the atmosphere in small-scale interaction [in Russian]. *Izvestiya, Atmospheric and Oceanic Physics*, *10*, 1110–1113.
Knuteson, R. O., Revercomb, H. E., Best, F. A., Ciganovich, N. C., Dedecker, R. G., Dirkx, T. P., et al. (2004). Atmospheric emitted radiance interferometer, Part II: Instrument performance. *Journal of Atmospheric and Oceanic Technology*, *21*, 1777–1789.
Lee, Z., Hu, C., Shang, S., Du, K., Lewis, M., Arnone, R., et al. (2013). Penetration of UV-visible solar radiation in the global oceans: Insights from ocean color remote sensing. *Journal of Geophysical Research: Oceans*, *118*, 4241–4255. https://doi.org/10.1002/jgrc.20308
Levitus, S., Antonov, J. I., Boyer, T. P., Baranova, O. K., Garcia, H. E., Locarnini, R. A., et al. (2012). World ocean heat content and thermosteric sea level change (0–2000 m), 1955–2010. *Geophysical Research Letters*, *39*, L10603. https://doi.org/10.1029/2012GL051106
Liu, W., & Businger, J. A. (1975). Temperature profile in the molecular sublayer near the interface of a fluid in turbulent motion. *Geophysical Research Letters*, *2*(9), 403–404.
Liu, W., Katsaros, K. B., & Businger, J. A. (1979). Bulk parameterization of air-sea exchanges of heat and water vapor including the molecular constraints at the interface. *Journal of the Atmospheric Sciences*, *36*, 1722–1734.
Liu, Y., Chin, M., & Minnett, P. J. (2017). Sampling errors in satellite-derived infrared sea-surface temperatures. Part II: Sensitivity and parameterization. *Remote Sensing of Environment*, *198*, 297–309.
Liu, Y., & Minnett, P. J. (2016). Sampling errors in satellite-derived infrared sea-surface temperatures, Part I: Global and regional MODIS fields. *Remote Sensing of Environment*, *177*, 48–64.
Lumpkin, R., Centurioni, L., & Perez, R. (2016). Fulfilling observing system implementation requirements with the global drifter array. *Journal of Atmospheric and Oceanic Technology*, *33*, 685–695.
MacDougall, A. H., Swart, N. C., & Knutti, R. (2017). The uncertainty in the transient climate response to cumulative CO_2 emissions arising from the uncertainty in physical climate parameters. *Journal of Climate*, *30*, 813–827.
McAlister, E. D., & McLeish, W. (1969). Heat transfer in the top millimeter of the ocean. *Journal of Geophysical Research*, *74*(13), 3408–3414.
Minnett, P. J. (2003). Radiometric measurements of the sea-surface skin temperature—The competing roles of the diurnal thermocline and the cool skin. *International Journal of Remote Sensing*, *24*, 5033–5047.
Minnett, P. J., Knuteson, R. O., Best, F. A., Osborne, B. J., Hanafin, J. A., & Brown, O. B. (2001). The marine-atmospheric emitted radiance interferometer: A high accuracy, seagoing infrared spectroradiometer. *Journal of Atmospheric and Oceanic Technology*, *18*, 994–1013.
Minnett, P. J., Smith, M., & Ward, B. (2011). Measurements of the oceanic thermal skin effect. *Deep Sea Research Part II: Topical Studies in Oceanography*, *58*(6), 861–868.
Miyahara, Y., & Aoshima, T. (2015). Advanced calibration of pyrgeometer by blackbody radiation with least squares technique applied to an improved steady state equation of heat transfer. *SOLA*, *11*, 70–74.
Moum, J. N., Caldwell, D. R., & Paulson, C. A. (1989). Mixing in the equatorial surface layer and thermocline. *Journal of Geophysical Research*, *94*(C2), 2005–2022. https://doi.org/10.1029/JC094iC02p02005
O'Carroll, A. G., Eyre, J. R., & Saunders, R. W. (2008). Three-way error analysis between AATSR, AMSR-E, and in situ sea surface temperature observations. *Journal of Atmospheric and Oceanic Technology*, *25*, 1197–1207.
Ohring, G., Wielicki, B., Spencer, R., Emery, B., & Datla, R. (2005). Satellite instrument calibration for measuring global climate change: Report of a workshop. *Bulletin of the American Meteorological Society*, *86*, 1303–1313.
Paulson, C., & Simpson, J. (1977). Irradiance measurements in the upper ocean. *Journal of Physical Oceanography*, *7*, 952–956.
Philipona, R., Fröhlich, C., Dehne, K., DeLuisi, J., Augustine, J., Dutton, E., et al. (1998). The Baseline Surface Radiation Network pyrgeometer round-robin calibration experiment. *Journal of Atmospheric and Oceanic Technology*, *15*(3), 687–696.
Ramanathan, V., Lian, M. S., & Cess, R. D. (1979). Increased atmospheric CO_2: Zonal and seasonal estimates of the effect on the radiation energy balance and surface temperature. *Journal of Geophysical Research*, *84*(C8), 4949–4958.
Rodgers, C. D. (2004). *Inverse methods for atmospheric sounding: Theory and practice* (2nd ed., 256 pp.). Singapore: World Scientific.
Rothman, L. S., Gordon, I. E., Babikov, Y., Barbe, A., Benner, D. C., Bernath, P. F., et al. (2013). The HITRAN2012 molecular spectroscopic database. *Journal of Quantitative Spectroscopy & Radiative Transfer*, *130*, 4–50.
Saunders, P. M. (1967). The temperature at the ocean-air interface. *Journal of Atmospheric Sciences*, *24*, 269–273.
Scanlon, B., Wick, G. A., & Ward, B. (2013). Near-surface diurnal warming simulations: Validation with high resolution profile measurements. *Ocean Science*, *9*(6), 977–986. https://doi.org/10.5194/os-9-977-2013

Soloviev, A., & Lukas, R. (1997). Observation of large diurnal warming events in the near-surface layer of the western equatorial Pacific warm pool. *Deep Sea Research Part I: Oceanographic Research Papers*, *44*, 1055–1076.

Soloviev, A., & Lukas, R. (2014). Near-surface turbulence. In *The near-surface layer of the ocean* (pp. 153–224). Dordrecht, the Netherlands: Springer.

Soloviev, A. V., & Schlüssel, P. (1994). Parameterization of the cool skin of the ocean and of the air-ocean gas transfer on the basis of modeling surface renewal. *Journal of Physical Oceanography*, *24*, 1339–1346.

Stokes, G. M., & Schwartz, S. E. (1994). The Atmospheric Radiation Measurement (ARM) Program: Programmatic background and design of the cloud and radiation test bed. *Bulletin of the American Meteorological Society*, *75*(7), 1201–1221.

Sutherland, G., Marié, L., Reverdin, G., Christensen, K. H., Broström, G., & Ward, B. (2016). Enhanced turbulence associated with the diurnal jet in the ocean surface boundary layer. *Journal of Physical Oceanography*, *46*(10), 3051–3067. https://doi.org/10.1175/JPO-D-15-0172.1

Sutherland, G., Reverdin, G., Marié, L., & Ward, B. (2014). Mixed and mixing layer depths in the ocean surface boundary layer under conditions of diurnal stratification. *Geophysical Research Letters*, *41*, 8469–8476. https://doi.org/10.1002/2014GL061939

Veron, F., Melville, W. K., & Lenain, L. (2011). The effects of small-scale turbulence on air-sea heat flux. *Journal of Physical Oceanography*, *41*(1), 205–220.

Ward, B., Fristedt, T., Callaghan, A. H., Sutherland, G., Sanchez, X., Vialard, J., et al. (2014). The Air–Sea Interaction Profiler (ASIP): An autonomous upwardly rising profiler for microstructure measurements in the upper ocean. *Journal of Atmospheric and Oceanic Technology*, *31*(10), 2246–2267. https://doi.org/10.1175/JTECH-D-14-00010.1

Ward, B., Wanninkhof, R., Minnett, P. J., & Head, M. J. (2004). SkinDeEP: A profiling instrument for upper decameter sea surface measurements. *Journal of Atmospheric and Oceanic Technology*, *21*, 207–222.

Wong, E. W., & Minnett, P. J. (2016a). Retrieval of the ocean skin temperature profiles from measurements of infrared hyperspectral radiometers. Part I: Derivation of an algorithm. *IEEE Transactions on Geoscience and Remote Sensing*, *54*(4), 1879–1890.

Wong, E. W., & Minnett, P. J. (2016b). Retrieval of the ocean skin temperature profiles from measurements of infrared hyperspectral radiometers. Part II: Field data analysis. *IEEE Transactions on Geoscience and Remote Sensing*, *54*(4), 1891–1904.

Woods, S., Minnett, P. J., Gentemann, C. L., & Bogucki, D. J. (2014). Influence of the oceanic cool skin layer on global air-CO_2 flux estimates. *Remote Sensing of Environment*, *145*, 15–24.